Biomaterials Science

PAPER

Mario Moisés Alvarez, Grissel Trujillo-de Santiago *et al.*

Multimaterial chaotic printing of reinforced and prevascularized hydrogel filaments: Fabrication of mechanical robust constructs for long-term muscle tissue culture

ROYAL SOCIETY
OF **CHEMISTRY**

European
Society for
Biomaterials

PAPER

Check for updates

Multimaterial chaotic printing of reinforced and prevascularized hydrogel filaments: Fabrication of mechanical robust constructs for long-term muscle tissue culture†

Andrea Cavero-Arrivasplata, [ID] ‡[a,b,c] David Hyram Hernández-Medina,‡[a] Irving Isaí Rendón-Moreno,[a,d] Diego Alonso Quevedo-Moreno, [ID] [g] Dariush Ebrahimibagha, [ID] [a] Sanal Kozhiparambil Chandran, [ID] [f] Julio Ernesto Valdivia Silva, [ID] [b] Claudia Maribel Luna-Aguirre, [ID] [a,c,d] Mario Moisés Alvarez [ID] *[a,c,d,e] and Grissel Trujillo-de Santiago [ID] *[a,c,d,e]

Engineering vascularization in hydrogel constructs remains a significant challenge in tissue engineering. Prevascularized hydrogels, engineered with void channels, enhance cell viability but often lack the mechanical stability needed for long-term culture, which is crucial for proper tissue maturation. In this study, we introduce chaotic bioprinting—a chaos-enabled biofabrication strategy—to produce mechanically robust hydrogel pre-vascularized filaments (with inner void channels) suited for extended culture. Utilizing a Kenics Static Mixer (KSM) printhead with various inlets (4 or 8), we developed fibers with intercalated layers of a myoblast-laden gelatin methacryloyl (GelMA)-alginate bioink, a sacrificial material for channel formation, and a reinforcing alginate scaffold. By optimizing ink ratios, we maximized cell-laden compartments while reinforcing the fiber structure and embedding microchannels for efficient mass and gas transport. Mechanical testing and degradation analysis reveal that optimized fibers achieve sufficient resistance (elastic modulus = 12.8 kPa) to withstand extended periods of cell culture up to 21 days. Additionally, C2C12 myoblasts cultured within these prevascularized and reinforced hydrogel filaments maintained high cell viability (>90%) for more than 21 days and demonstrated superior cell proliferation, spreading, and alignment throughout the filament volume compared to solid fibers (reinforced but without inner void channels). Sacrificial layers created void microchannels, enhancing mass and gas transport, while the reinforcing layers provided structural integrity. Multimaterial chaotic printing enabled the fabrication of mechanically stable, functional constructs with compartmentalized architectures, facilitating extended culture and tissue maturation. Our results demonstrate the potential of this method for engineering thick tissues, including skeletal muscle, and highlight its versatility for various regenerative medicine applications, advancing biofabrication towards thicker and mature tissues.

*[a]Tecnologico de Monterrey, Escuela de Ingeniería y Ciencias, Ave. Eugenio Garza Sada 2501 Sur, Col: Tecnológico, Monterrey, N.L., México, 64700.
E-mail: grissel@tec.mx, mario.alvarez@tec.mx*
[b]Departamento de Bioingeniería, Universidad de Ingeniería y Tecnología de Lima, 15063, Lima, Peru
[c]Tecnologico de Monterrey, Expedition-FEMSA, Ave. Eugenio Garza Sada 2501 Sur, Col: Tecnológico, Monterrey, N.L., México, 64700
[d]Tecnologico de Monterrey, Monterrey, Departamento de Mecatrónica, Ave. Eugenio Garza Sada 2501 Sur, Col: Tecnológico, Monterrey, N.L., México, 64700
[e]Forma Foods, Research and Development Unit, Tecnológico de Monterrey, Monterrey, Nuevo León, 64849, Mexico
[f]Facultad de Ciencias Químicas, Universidad Autónoma de Nuevo León, San Nicolás de los Garza, Nuevo León, 66455, Mexico
[g]Department of Mechanical Engineering, Massachusetts Institute of Technology, Cambridge, MA, 02139, USA
†Electronic supplementary information (ESI) available. See DOI: https://doi.org/10.1039/d4bm01674b
‡These authors contributed equally to this work.

Introduction

Bioprinting holds great promise in creating functional tissues for diverse applications, from developing physiological models for foundational research[1–4] and *in vitro* pharmaceutical testing[4–9] to producing implantable tissues for patients[10–14] and even cultivated meat.[15–18] Hydrogels are frequently selected in these efforts,[19] as they mimic the extracellular matrix of mammalian tissue and provide an optimal environment for cell attachment and proliferation. Within the last decade, novel bioprinting techniques, including vat photopolymerization-based bioprinting[20,21] and electrohydrodynamic jet bioprinting,[22,23] have enabled the fabrication of high-resolution structures using hydrogels. However, achieving dense and mature tissue structures of a few cubic centimeters

remains challenging due to several technical limitations. One primary barrier is the need for vascularization within these bioprinted constructs.[24,25] Vascular structures play a vital role in sustaining cellular function by transporting nutrients, oxygenating cells, and removing waste.[25] Thus, to promote cellular growth and achieve tissue maturation, the inclusion of vascular-like channels is essential. Achieving hydrogel constructs that are both, porous enough to mimic vascular conduits and mechanically stable for extended culture is particularly challenging. Hydrogels, especially those with internal channels, are soft and prone to erosion,[26] often limiting their use in long-term cell culture.

Recent advances in chaotic bioprinting offer a promising approach to overcoming these limitations. Continuous chaotic bioprinting[27–29] is a multi-material extrusion technique that uses chaotic flows to generate multi-compartmentalized hydrogel filaments with alternating layers of different materials.[30] This approach relies on using printheads equipped with Kenics Static Mixer (KSM) elements, which induce chaotic flows by iteratively reorienting and splitting the materials as they pass through the printhead.[30] In previous work, we have shown applications of chaotic printing in diverse scenarios, and we have demonstrated the versatility of the technique for printing more than two materials[31] to produce material constructs with a distinctive microstructure composed of multiple, alternating, and parallel layers of the different materials fed to the printhead. Moreover, using sacrificial inks, we previously demonstrated the ability to print hydrogel filaments with internal microchannels (capillary-size) in a single step, enhancing mass transport and improving metabolic activity and cell differentiation.[31,32] Despite these advantages, a significant limitation persists: the hydrogel filaments produced lack mechanical robustness, leading to degradation and erosion within a few days of culture. This instability restricts the construct's potential for extended culture, which is essential for achieving mature, functional tissues.[33]

In this study, we present an enhanced chaotic bioprinting approach designed to produce mechanically robust hydrogel filaments suitable for prolonged cell culture. Our strategy involves using a multi-port KSM printhead with multiple inlets (8 and 4) and two mixing elements to print hydrogel filaments with intercalated layers of myoblast-laden gelatin methacryloyl (GelMA)-alginate bioink, a sacrificial material to fabricate void channels, and a reinforcing alginate scaffold. This multimaterial design allows us to integrate the presence of cell-laden compartments, reinforce the fiber structure, and incorporate microchannels that facilitate efficient nutrient and gas exchange. By leveraging chaotic flows, we aimed for a construct architecture that balances prevascularization with enhanced mechanical stability, thus advancing biofabrication towards durable, mature tissue models.

The multimaterial printing strategy introduced in this study is versatile and can be adapted to fabricate a wide range of tissues. For the first proof-of-concept demonstration, we chose the fabrication of skeletal muscle fibers due to their relevance across various applications. Skeletal muscle tissue models are critical for fundamental studies on muscle physiology,[34,35] aging,[36] and muscle-related pathologies,[35,37,38] as well as for pharmacological testing.[35] Muscle tissue engineering will enable the fabrication of implantable muscle constructs,[39,40] and cultured meat production.[41] Additionally, skeletal muscle presents unique fabrication challenges, including its highly aligned architecture and the need for extended culture periods to achieve maturation under optimal nutrient and oxygen supply. These requirements align closely with the capabilities of our chaotic bioprinting approach, making skeletal muscle an ideal model to showcase the utility and effectiveness of this multimaterial printing technique.

Results and discussion

Fabrication of multimaterial hydrogel filaments

Here, we demonstrate a simple biofabrication strategy that renders mechanically robust prevascularized cell-laden hydrogel filaments that withstand culture conditions for extended times. Instead of relying on the addition of particles,[42] nanoparticles,[43] or supporting scaffolds,[44] we developed an inner scaffold while printing. For this, we rely on the multimaterial character of extrusion-based chaotic printing[31] and its ability to create well-organized multicompartmental microstructure.[30]

Here we illustrate the implementation of a multimaterial (bio)printing strategy to develop skeletal-muscle tissue-like fibers with internal prevascularization, made from soft and common hydrogel materials (i.e., alginate and GelMA)[45] that can withstand extended incubation periods (up to 28 days).

To develop these tissue constructs, we followed the following logical steps. First, in acellular experiments, we tested different feeding strategies of three distinct inks with complementary functionalities, namely a structural (scaffolding) ink, a sacrificial ink, and a cell-friendly ink. Then, in tensile tests, we evaluated the mechanical properties of hydrogel filaments obtained from these feeding strategies and selected those that exhibited higher young modulus for assessment of erosion resistance under benign agitation and incubation at 37 °C in culture medium. Finally, filament formulations with good performance in these erosion experiments were used in bioprinting experiments in which murine myoblasts were integrated in cell-friendly inks. We evaluated the performance of these constructs through 28 days of culture in terms of viability, metabolic activity, cell density, cell alignment, and muscle tissue maturation.

In chaotic printing, the number and location of these layers can be determined a priori by selecting a suitable geometry of the printhead (i.e., number of mixing elements and number of inlets).[29,31,46] In a first set of acellular experiments, we used chaotic printheads equipped with 8 inlets and two KSM elements (Fig. 1A) to coextrude three different inks, namely a structural ink composed of 4% high-viscosity alginate (Alg_H), a cell-friendly ink composed of 3% GelMA and 3.5% low-viscosity alginate (Alg_L), and a sacrificial ink consisting of 0.6% hydroxyethyl cellulose (HEC) (Fig. 1Bi). This printhead con-
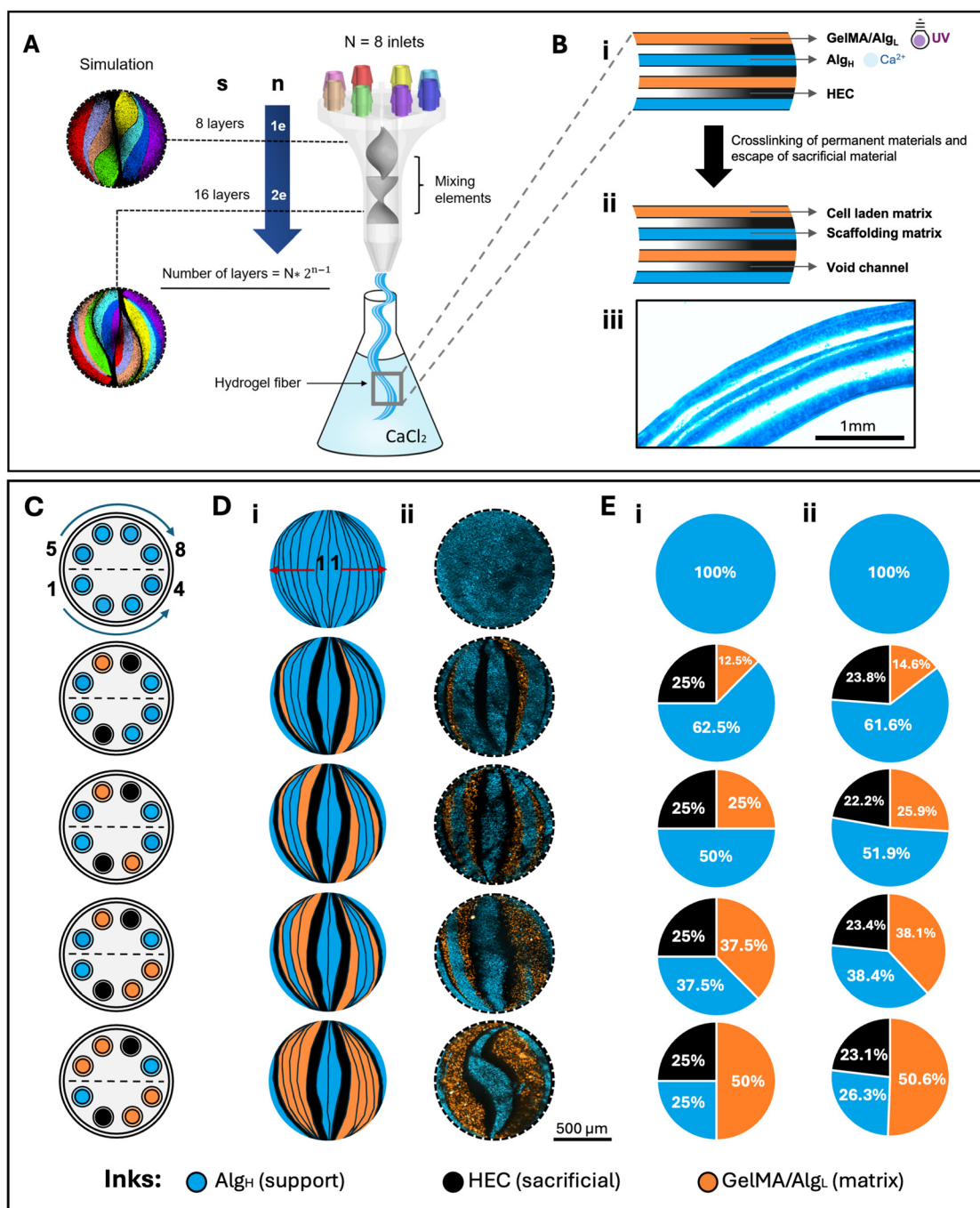
Fig. 1 Printing setup and architectural characterization. (A) Schematic representation of continuous chaotic bioprinting using the 8-inlet, 2-KSM-element printhead. Feeding eight inks into this setup produces hydrogel filaments with 16 intercalated layers. The first KSM element reorients the feeding streams, maintaining 8 compartments at the cross-section corresponding to the end of the first KSM element. The second KSM element splits each compartment, generating 16 alternating layers at the printhead outlet. Alginate-based inks are crosslinked upon extrusion by extruding the filaments in a calcium chloride solution. (B) Three distinct inks used in this study: a sacrificial ink (black), a scaffolding ink for mechanical support (blue), and a cell-friendly ink (orange). This combination enables the fabrication of: (i) Multimaterial hydrogel filaments with compartments for cell growth, mechanical reinforcement, and nutrient/gas perfusion. (ii) Prevascularized filaments with inner void microchannels, formed by the leaching of the sacrificial ink after crosslinking the permanent materials. (iii) Lateral view under brightfield microscopy of a prevascularized filament composed of 4% Alg_H and loaded with fluorescent particles. Transparent longitudinal void channels are visible along the filament's length. (C) Variation in ink proportions across experiments, maintaining a consistent sacrificial ink proportion (2 of 8 inlets) for all hollow fibers. The numbering of inlets (1–8) corresponds to the successive order in which layers of different materials will appear within the printed hydrogel filament. (D) Cross-sectional comparison of: (i) Conceptual designs and (ii) experimental results of solid alginate fibers loaded with fluorescent microparticles. Arrows indicate the expected sequence of compartments (from 1 to 8), matching the inlet assignment order described in (C). (E) Area fraction analysis of inks in the filament cross-section, comparing: (i) Conceptual and (ii) experimental results. Proportions were calculated by measuring the area of each ink (light blue, orange, black) relative to the total cross-sectional area.

figuration rendered compartmentalized fibers with 16 intercalated layers (Fig. S1†) of the feed materials because the eight feeding streams are reoriented by the first mixing elements and then split by the second mixing element.

Since the multimaterial filament was extruded through a nozzle orifice of 1 mm, each layer exhibits, on average, a thickness of 62.5 μm (1000 μm/16) at the central line of the cross-section. The printing process involved submerging the printhead outlet directly into a calcium chloride ($CaCl_2$) bath to crosslink the alginate molecules, followed by UV light exposure to stabilize the GelMA matrix.

The composition of the sacrificial and cell-loadable inks were determined based on previous reports of our group.[32] The scaffolding ink composition was a 4% alginate-based ink.

Our selection of 4% Alg_H solution as a scaffolding ink was based on preliminary assays that demonstrate that the use of 6% Alg_H results in brittle constructs, while the use of 2% Alg_H results in a significantly weak fiber. Therefore 4% Alg_H was selected for the subsequent experiments. Indeed, combining alginate with collagen or gelatin to create a mixed bioink is one common approach to improve mechanical strength of scaffolds.[47–49] However, here we can micro-compartmentalize our stiffest alginate-based fibers to provide the desired mechanical support, without compromising the compartments loadable with living cells which must be softer and looser matrices. The sacrificial ink, composed of 0.6% (w/v) HEC, leached out during crosslinking to create hollow microchannels to enhance nutrient and gas exchange along the filament's length (Fig. 1Bii).

In chaotic printing, the relative location of the inner layers can be determined *a priori* by selecting a suitable feeding position for each one of the materials to be used (see also Fig. S1†).[31,50] Fig. 1B shows the rationale of the architectural design of our fibers. With the selection of three hydrogel-based materials or inks, we aimed to continuously fabricate long hydrogel filaments containing a compartmentalized architecture composed of multiple repetitions of a sequence of three different material environments, namely solid layers for enhancing mechanical robustness, solid layers suitable for cell proliferation, and sacrificial layers to create prevascularization. Fig. 1Biii shows a brightfield micrograph of a fiber containing inner hollow microchannels and reinforced with Alg_H. Light layers correspond to the hollow microchannels produced by the leaching of the sacrificial material, while blue layers correspond to 4% Alg_H loaded with colored particles.

We explored a wide variety of formulations and feeding configurations (see Fig. 1C–E; Table 1), their effect on the mechanical properties of the printed fibers and their stability under extended culture conditions.

Of note, achieving multimaterial filaments with precise architecture required careful optimization of flow conditions. Preliminary experiments revealed that, as the number of materials increased, the flow rate needed to decrease to produce fibers with distinct material compartments. The selection of proper flow rates ensured that the inks behaved as Newtonian fluids, resulting in the preservation of the expected multilayered microstructures that are characteristic of chaotic printing and mechanically stable fibers (Table 1). Indeed, using a flow rate of 0.20 mL min⁻¹ produced consistent fibers with clear structural integrity. However, deviations from this rate led to non-Newtonian behavior, nozzle clogging, and irregularities in the printed fibers, compromising their multilayered microstructure or mechanical stability, or both.

To assess the effects of these parameters on mechanical properties and integrity under culture conditions, various formulations and/or configurations were tested, including a solid fiber composed solely of the structural ink as a control (Table 1, Fig. 1D and E). The design strategy also aimed to ensure that cell-laden compartments were adjacent to sacrificial layers, with inter-layer distances not exceeding 200 μm to prevent mass transfer limitations that could impair cell viability. The 62.5 μm layer width achieved by the bioprinting setup, combined with the placement of cell-containing layers near the void channels, effectively addressed these constraints. Originally, we aimed to maximize the number of cell-laden compartments, while striving to distribute structural compartments evenly and minimize their volumetric fraction. Computational simulations guided the rational pre-design of the filament architecture by predicting the placement of materials based on input configurations (see Fig. S1†). Then, we printed solid fibers using color inks (*i.e.*, three distinct inks, each containing solid particles of a dis-

Table 1 Materials and flow rates used for printing

| Type of KSM | Type of fiber | Type of material | | Sacrificial | Flow rate (mL min⁻¹) |
		Support	Matrix		
8 inlets, 2 mixing elements	Solid	2% Alg_H	—	—	1.00
	Hollow	2% Alg_H	—	0.6% HEC	0.50
		2% Alg_H	3% GelMA/3.5% Alg_L	0.6% HEC	0.20
		2% Alg_H	3% GelMA/3.5% Alg_L + 3×10^6 cells per mL	0.6% HEC	0.15
2 inlets, 4 mixing elements	Solid	—	3% GelMA/3.5% Alg_L	—	1.00
		4% Alg_H	3% GelMA/3.5% Alg_L	—	0.75
	Hollow	—	3% GelMA/3.5% Alg_L	0.6% HEC	0.60

All concentrations are % (w/v).

tinct color) and demonstrated the similarity between the anticipated and experimental cross-sections (Fig. 1Di and Dii). Image analysis of the area fractions occupied by the different inks further corroborated the consistency between

pre-designed and experimental outcomes (Fig. 1Ei and Eii). These findings highlight the robustness of the proposed printing setup for designing complex multimaterial architectures.
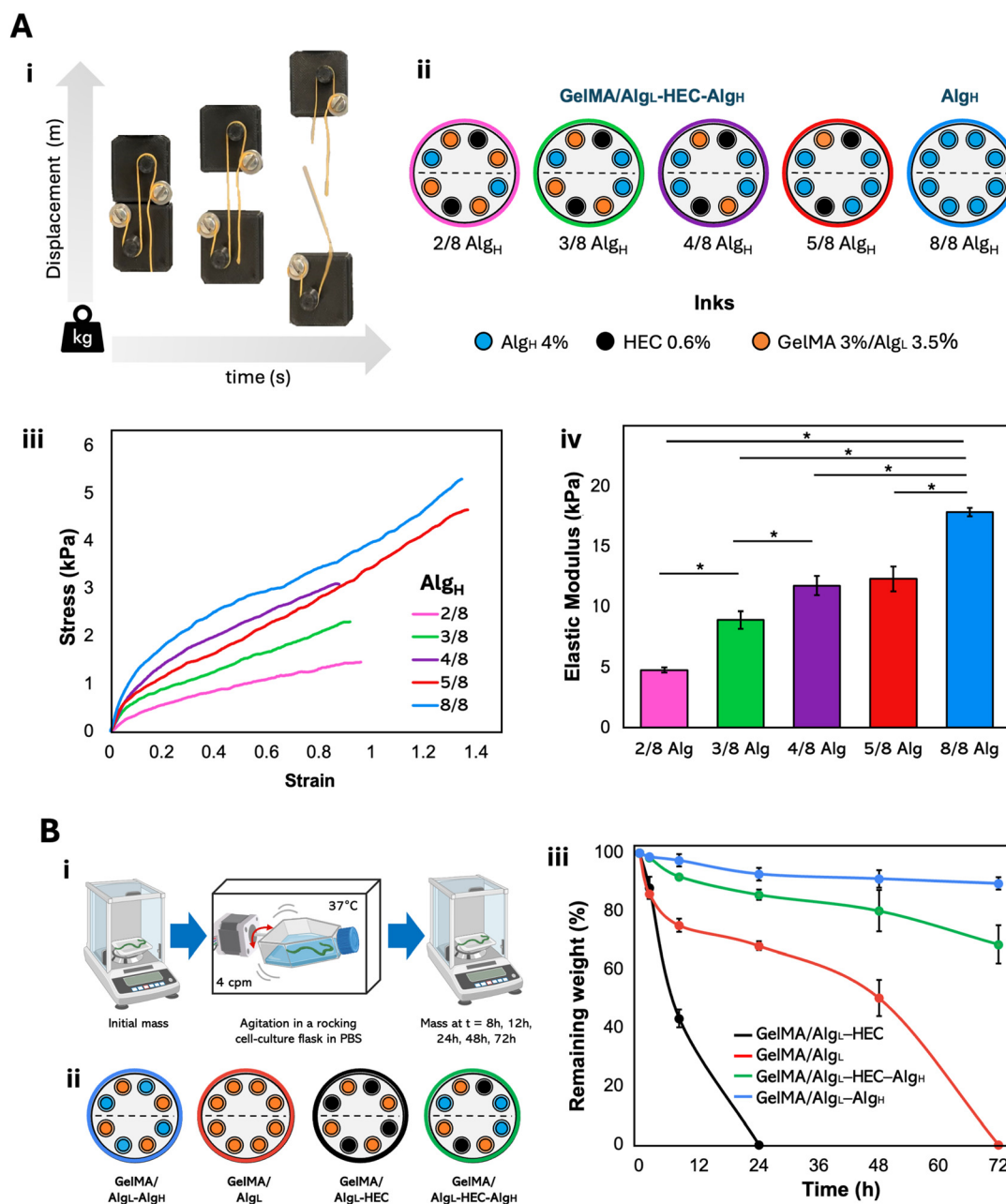

Fig. 2 Mechanical properties and stability under simulated culture conditions. (A) Determination of the mechanical properties of multichannel hollow fibers through tensile assays. (i) Tensile assays were done using a universal tensile machine with a load of 1 kg, in which the displacement in the y-axis increases in time until the fiber breaks. (ii) Scheme of the inlet design of the KSM printhead, featuring 8 inlets and 2 mixing elements, which was used to print fibers for mechanical analysis. (iii) Stress–strain curves of fibers with 2/8, 3/8, 4/8, 5/8, and 8/8 inlets with Alg_H. (iv) Young's modulus of each fiber, obtained by calculating the slope of the stress–strain curve. (B) Determination of fibers stability under simulated culture conditions. (i) Schematic representation illustrating the experimental setup used to evaluate the stability of printed fibers under simulated dynamic culture conditions in a rocking cell-culture flask. (ii) Printhead configuration used to print fibers for degradation analysis. (iii) Remaining weight of fibers in the first 72 hours of agitation in a rocking cell-culture flask. Hollow fibers of $GelMA/Alg_L$-HEC (black) degraded after 24 h, and solid fibers of just $GelMA/Alg_L$ (red) degraded after 72 hours, whereas hollow fibers of $GelMA/Alg_L$-HEC-Alg_H (green), and solid fibers of $GelMA/Alg_L$-Alg_H (blue) remained with more than 70% of their initial mass after the same time. Statistical significance (*) with $p < 0.01$ and $n = 3$.

Mechanical properties of multimaterial filaments

Aiming to identify a fair compromise between structural integrity and the number of cell-friendly or void compartments within hydrogel filaments, we evaluated the mechanical properties of various formulations and architectures using tensile testing. These tests were conducted using a custom-built universal tensile testing device. The tensile setup is illustrated in Fig. 2Ai and Aii shows the scheme of the inlet design of the KSM printhead, which was used to print fibers for mechanical analysis.

The structural ink (4% Alg_H) was fed into the chaotic printhead at varying proportions, ranging from 2/8 to 5/8 of the total inlets, with the remaining inlets allocated to sacrificial ink (0.6% HEC) and cell-loadable ink (3% GelMA/3.5% Alg_L). A control composed entirely of Alg_H (8/8) was also included for comparison. Continuous structured filaments were successfully produced with higher proportions of sacrificial ink (up to 3/8), but these constructs were mechanically weaker, exhibiting tensile strengths below 9 kPa (Fig. 2Aiii and Table 2).

Stress–strain curves for each configuration (Fig. 2Aiii) and their corresponding elastic modulus values (Fig. 2Aiv) revealed a clear trend: the inclusion of Alg_H layers significantly enhanced the mechanical robustness of the hydrogel filaments. Notably, filaments composed entirely of Alg_H (8/8) had the highest elastic modulus, reaching 17.87 kPa. This value was statistically different from all other configurations, confirming the critical role of Alg_H in providing mechanical reinforcement.

Interestingly, filaments with 5/8 and 4/8 Alg_H proportions did not exhibit statistically significant differences in elastic modulus, whereas those with 4/8 and 3/8 Alg_H proportions showed significant differences. These results suggest that the mechanical reinforcement provided by the scaffolding ink (4% Alg_H) follows an asymptotic trend, with diminishing returns when more than half of the inlets are dedicated to the structural ink.

In the context of practical applications, filaments with 3/8 and 4/8 Alg_H were considered suitable for experiments invol-

ving living cells, as they offered a good balance between mechanical stability and the availability of cell-loadable compartments (3 and 2 compartments, respectively). Ultimately, we selected the 3/8 Alg_H configuration, which demonstrated an elastic modulus of approximately 8.93 kPa, for subsequent experiments. This configuration provided a higher number of GelMA/Alg_L layers, maximizing the potential for cell hosting while maintaining sufficient mechanical stability for extended culture.

To evaluate the resistance of the optimized hydrogel filament (3/8 Alg_H) to degradation under dynamic conditions, we conducted erosion assays in a rocking cell-culture flask. This system generates a gentle, cyclic movement with low shear stress, simulating benign agitation conditions akin to those encountered in tissue culture bioreactors. The flask completes one cycle of movement, consisting of a half rotation, in one minute (Fig. 2Bi).

The susceptibility of the fibers to erosion was assessed by measuring the percentage of remaining filament mass over time. For comparison, we included three control samples printed using the KSM printhead configurations shown in Fig. 2Bii. These controls comprised (a) a solid fiber reinforced with alginate (3% GelMA/3.5% Alg_L + 4% Alg_H), (b) a solid fiber without alginate reinforcement (3% GelMA/3.5% Alg_L), and (c) a hollow fiber without alginate reinforcement (3% GelMA/3.5% Alg_L + 0.6% HEC) (Fig. 2Bii).

The test sample was the optimized multimaterial hollow fiber (3% GelMA/3.5% Alg_L + 0.6% HEC + 4% Alg_H) that was selected from the mechanical characterization experiments in virtue of demonstrating superior mechanical properties and contained reinforcing Alg_H layers, cell-friendly GelMA/Alg_L layers, and sacrificial HEC layers to create hollow channels.

Erosion testing results clearly demonstrated the importance of alginate reinforcement in resisting erosion under continuous agitation. Hydrogel filaments with void channels and without alginate reinforcement (GelMA/Alg_L + HEC) completely degraded after 24 hours, while solid filaments without reinforcement (GelMA/Alg_L) degraded entirely after 72 hours. In contrast, both solid fibers with alginate reinforcement (GelMA/Alg_L + Alg_H) and hollow fibers with alginate reinforcement (GelMA/Alg_L + HEC + Alg_H) retained over 75% of their initial mass after 72 hours of continuous agitation (Fig. 2Biii).

Of note, despite the presence of structural reinforcement, prevascularized filaments with alginate layers experienced more mass loss compared to solid reinforced filaments. This should be mainly attributed to the presence of internal channels within the hydrogel filaments which facilitates perfusion and erosion along the inner walls of the construct.

These findings underscore the significance of alginate content in enhancing mechanical stability and resistance to erosion. The higher alginate proportion in reinforced solid fibers (4/8 Alg_H) conferred greater mass retention under agitation compared to hollow fibers with a lower alginate pro-

Table 2 Tensile assay results

	Strain at break	Stress at break (kPa)	Elastic modulus (kPa)
Proportion of HEC			
2/8 inlets	0.49 ± 0.14	2.15 ± 0.16	10.74 ± 0.05
4/8 inlets	0.76 ± 0.16	3.10 ± 0.28	11.76 ± 1.03
6/8 inlets	0.32 ± 0.08	1.32 ± 0.52	9.44 ± 0.08
Proportion of Alg_H			
2/8 inlets	1.05 ± 0.15	1.52 ± 0.13	4.78 ± 0.72
3/8 inlets	1.07 ± 0.14	2.55 ± 0.21	8.93 ± 0.81
4/8 inlets	0.76 ± 0.16	3.10 ± 0.28	11.76 ± 1.03
5/8 inlets	1.52 ± 0.13	4.34 ± 0.32	12.33 ± 0.36
8/8 inlets	1.29 ± 0.24	6.73 ± 1.25	17.87 ± 0.21
Concentration of Alg_H			
2% (w/v)	1.07 ± 0.16	2.55 ± 0.28	8.93 ± 1.03
4% (w/v)	1.54 ± 0.02	6.96 ± 0.45	12.80 ± 0.44
6% (w/v)	0.86 ± 0.34	7.05 ± 2.84	25.83 ± 0.25

portion (3/8 Alg_H). However, the inclusion of channels in the hollow fibers offers critical advantages for mass transfer and prevascularization, justifying their use for long-term tissue culture applications despite their slightly reduced erosion resistance.

Fabrication of reinforced multichannel muscle-like fibers: Comparison of reinforced solid and hollow filaments in cell-laden bioprinting

Degradation studies demonstrated that hydrogel filaments reinforced with 3/8 of 4% Alg_H could retain their mass and structural integrity after three days of continuous agitation. Based on these results, we selected this filament configuration for subsequent bioprinting experiments. In these experiments, we used reinforced fibers containing 3/8 of 4% Alg_H, 2/8 of sacrificial ink (0.6% HEC), and a C2C12 cell-laden ink composed of 3×10^6 cells per mL suspended in a 3% GelMA/3.5% Alg_L blend (Fig. 3Ai). For comparison, we also bioprinted solid hydrogel filaments reinforced with Alg_H layers but without sacrificial inks (Fig. 3Aii).

As anticipated, incorporating cells into the GelMA/Alg_L matrix slightly increased the apparent viscosity (ESI Fig. S2†), likely due to particle–matrix interactions introduced by suspended cells. This increase in viscosity required empirical adjustments in flow rate to maintain high-quality filament formation. Specifically, we reduced the extrusion flow rate by approximately 25%—from 0.20 mL min^{-1} to 0.15 mL min^{-1}—to maintain consistent filament formation and avoid overpressure at the nozzle, which could otherwise result in irregular deposition or excessive shear stress on the cells. These adjustments also enabled the reproducible production of filaments with a well-defined compartmentalized architecture.

The resulting muscle tissue-like filaments featured internal void channels to enhance mass transport, critical for maintaining cell viability and promoting tissue maturation (Fig. 3Aiii). The cell-laden hydrogel fraction provided a soft matrix conducive to cell anchorage, proliferation, and differentiation—essential for the transformation of myoblasts into multinucleated muscle cells.[32,49,51,52] Sacrificial ink layers leached out during crosslinking, creating hollow microchannels along the filament's length to enhance nutrient and gas exchange. Chaotic bioprinting enabled these materials to be arranged in intercalated parallel layers, closely mimicking the highly aligned, organized, and compartmentalized architecture of skeletal muscle (Fig. 3Aiv). We hypothesized that this architecture would favor tissue maturation, resulting in skeletal muscle tissue-like filaments after extended culture.

To evaluate the functionality of the fabricated filaments, we compared cell viability, cell density, cell proliferation, and alignment between reinforced solid and hollow fibers (Fig. 3B and C). While solid reinforced filaments were expected to demonstrate superior mechanical robustness throughout culture, we hypothesized that hollow fibers would outperform solid ones in terms of cell viability and proliferation. The enhanced mass transfer facilitated by the void channels eliminates nutrient and oxygen transport limitations in the hydrogel core, creating a more favorable environment for cell growth and differentiation.

Indeed, reinforced prevascularized filaments exhibited significantly higher cell viability (>80%) compared to solid filaments at all time points (days 1, 7, and 14; Fig. 3B). Cell viability in hollow fibers increased during the first 14 days of culture, reaching values above 98% by day 14. In contrast, solid filaments showed an initial increase in cell viability between days 1 and 7, plateauing at approximately 80% by day 14.

Interestingly, no significant differences in cell density were observed between the two filament types during the first week of culture. However, by day 14, cell density (defined as the number of living cells per unit volume) was significantly higher in hollow filaments compared to solid ones (Fig. 3C).

Notably, in solid fibers, viable cells predominantly resided in the outer sections of the filaments, with more than 95% of the live cells located within 200 μm of the filament surface. Z-Stack microscopy images confirmed remarkable cell proliferation near the surface of solid fibers, with minimal cell presence deeper within the filament core (Fig. 3D). In contrast, hollow filaments supported cell proliferation throughout their entire volume. Z-stack images encompassing the entire thickness of the hollow filaments revealed evenly distributed cells across the cross-section, indicating that the void channels improved mass transfer and supported cell viability and proliferation throughout the construct (Fig. 3E).

These results highlight the advantages of incorporating void microchannels in reinforced hydrogel filaments. The presence of void channels significantly improves cell viability and proliferation in mechanically stable constructs, making them suitable for extended culture and possibly tissue maturation.

In the following set of experiments, we investigated how different printhead configurations and degrees of compartmentalization affected the alignment, proliferation, and maturation of muscle-like fibers. Specifically, we compared hydrogel filaments fabricated using printheads with 4 inlets and 2, 4, or 6 KSM elements. As a control, we also bioprinted filaments using single-inlet printheads where the supportive ink, sacrificial ink, and C2C12 cells in the GelMA/Alg_L blend were fully mixed before extrusion.

Cell viability trends mirrored previous observations: cells in hydrogel filaments without void channels (single-inlet printheads) localized primarily near the filament surface, whereas cells in prevascularized filaments with void channels proliferated throughout the entire volume during extended culture (Fig. 4A and B). Reinforced and prevascularized filaments consistently maintained >95% cell viability over 21 days with minimal erosion (Fig. 4Ai and Aii).

Remarkably, filaments with eight or more compartments exhibited significant cell alignment. Confinement within
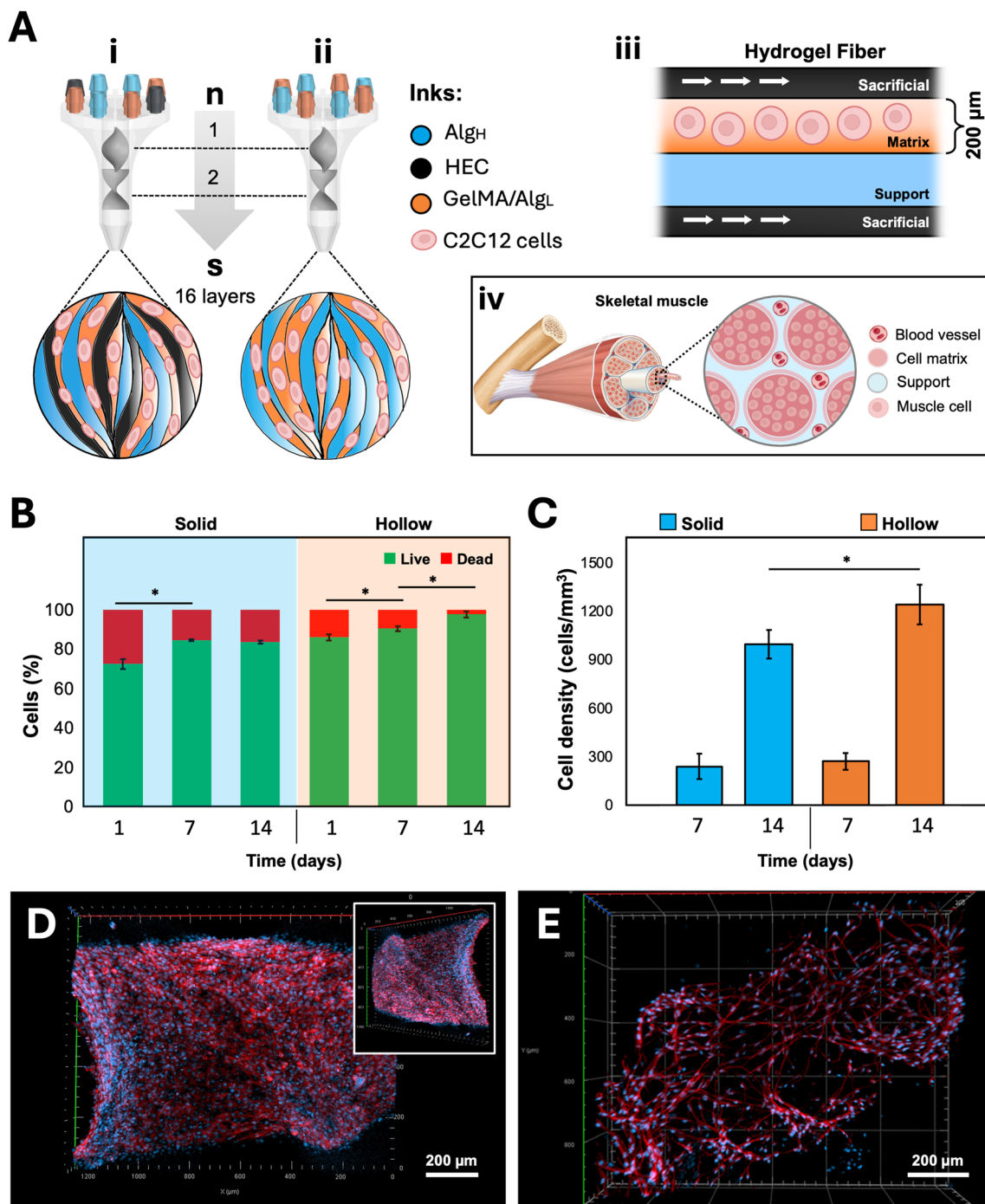
Fig. 3 Culture conditions and performance of chaotically printed cell-laden hydrogel fibers. (A) Schematic representation of the printhead configurations and feeding points used for fabricating hydrogel fibers. (i) Prevascularized filaments containing 4% Alg_H, 0.6% HEC and 3% GelMA/3.5% Alg_L with C2C12 cells were fabricated using a KSM with 8 inlets and 2 mixing elements. (ii) Solid fibers composed of 4% Alg_H and 3% GelMA/3.5% Alg_L with C2C12 cells were fabricated using a KSM with 8 inlets and 2 mixing elements. Both strategies yielded hydrogel fibers with 16 intercalated layers, where GelMA/AlgL layers were flanked by Alg_H layers for mechanical support. In the case of prevascularized filaments, HEC layers were additionally included to create void channels upon leakage. (iii) Schematic representation of the longitudinal architecture of the printed fiber, showing the functional organization of sacrificial channels, the cell-laden matrix, and the structural support compartment. (iv) Microarchitecture of skeletal muscle tissue for comparison.

layers narrower than 125 μm appeared to promote multinucleation and alignment, particularly in prevascularized fibers fabricated using 6-KSM-element printheads (Fig. 4B and C). Homogeneous constructs with no compartments (*e.g.*, fibers fabricated using premixed inks extruded through a 1-inlet, 6-KSM-element printhead) showed negligible cell alignment, underscoring the importance of compartmentalization for achieving muscle-like fiber architecture.
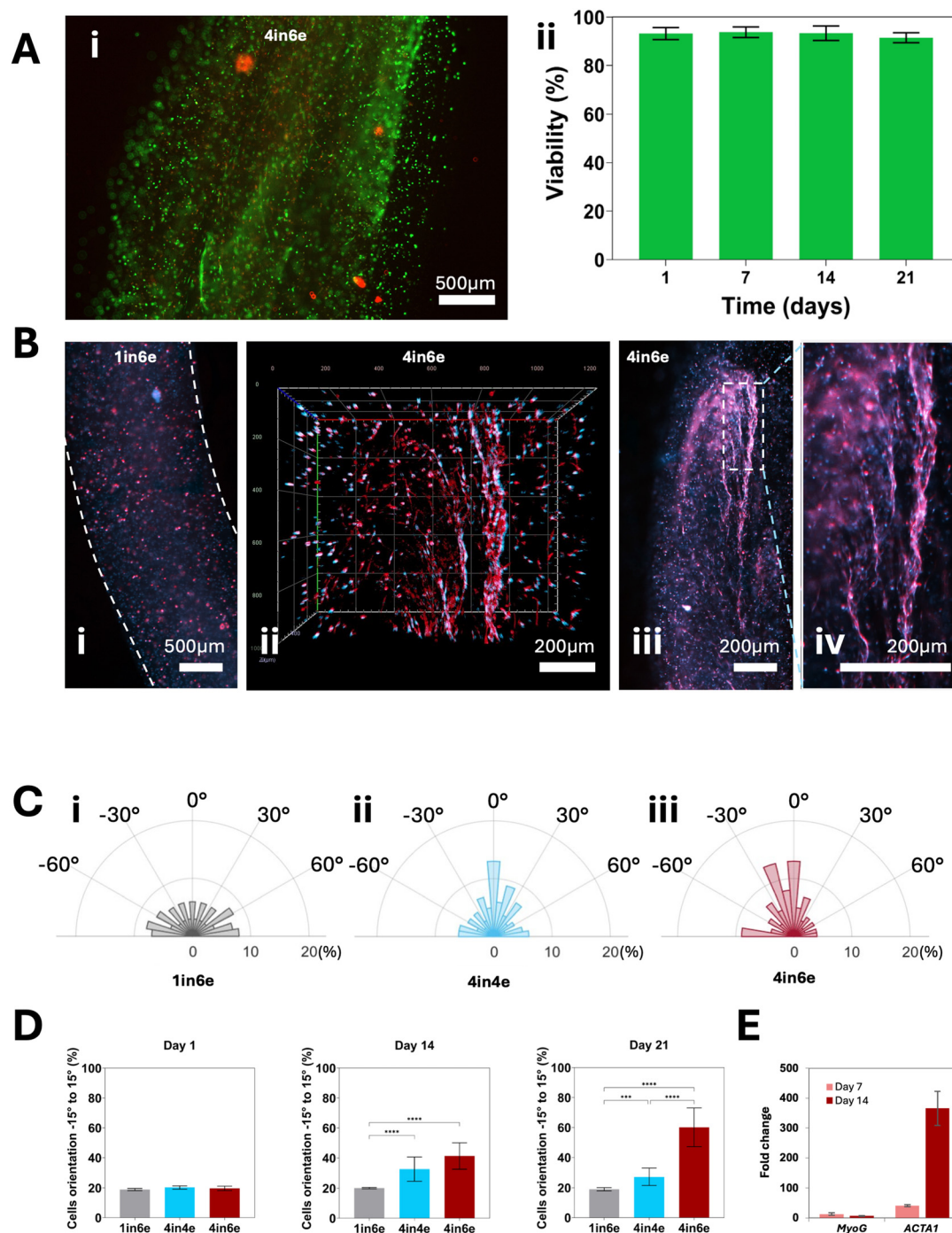
Fig. 4 Enhanced alignment of C2C12 cells in prevascularized and mechanically reinforced hydrogel filaments. (A) Viability assessment of C2C12 cell-laden, prevascularized, and mechanically reinforced hydrogel filaments during 21 days of culture. (i) Representative microscopy image showing Live/Dead staining after 21 days of culture. (ii) Quantitative analysis of cell viability throughout the 21-day culture period. (B) Microscopy images of Actin/DAPI staining of prevascularized and reinforced C2C12 cell-laden hydrogel filaments after 21 days of culture. Constructs were bioprinted with the exact same composition using a chaotic printhead with (i) one inlet and six KSM elements (1in6e) and (ii–iv) four inlets and six KSM elements (4in6e; all inks pre-mixed). (ii) Z-Stack of 2D longitudinal images illustrating high cell density and alignment across the filament volume. (iii) Longitudinal section showing a high degree of cell alignment. (iv) Close-up image highlighting the length and alignment of muscle-like fibers. (C) Comparison of cell alignment in constructs fabricated using different printing strategies. (i) Solid filaments printed using 1in6E showed negligible cell alignment. Prevascularized and reinforced filaments bioprinted using chaotic printheads with 4 inlets and (ii) 4 or (iii) 6 KSM elements demonstrated significant cell alignment. (D) Percentage of multinucleated cells aligned within ±15° of the filament's main axis over a 21-day culture period. The X-axis labels indicate the printhead configurations (*e.g.*, *1in6e* indicates the use of a single-inlet printhead with 6 KSM elements). In single-inlet experiments, all inks were pre-mixed before extrusion. (E) Relative expression levels of *MyoG* and *ACTA1*, two markers of myogenic differentiation, at days 7 and 14 in filaments printed using the 4in6e configuration (*n* = 3), as measured by RT-qPCR assays. A marked upregulation was observed at day 14, consistent with progressive myogenic maturation.

These results highlight the dual role of void channels and compartmentalization in facilitating cell alignment (Fig. 4C and D). Void channels improved mass transfer, eliminating nutrient and oxygen limitations, while compartmentalization constrained cells within discrete layers, fostering interactions necessary for alignment and multinucleation. Solid filaments, by contrast, exhibited limited cell spreading and alignment confined to their surface. Prevascularized filaments supported cell alignment and spreading throughout their volume, demonstrating the importance of structural reinforcement with 4% Alg_H layers (Fig. 4D). In addition, we performed quantitative PCR (qPCR) to analyze the expression of specific muscle-related biomarkers, *MyoG* and *ACTA1*. The expression patterns of these genes offer insights into the differentiation and maturation status of the myoblasts (Fig. 4E). *MyoG* and *ACTA1* are well-established indicators of myogenic differentiation,[53] signifying that the cells are progressing towards myotube formation.

In sum, the integration of void channels and compartmentalized architecture, enabled by chaotic bioprinting, proved critical for long-term culture and the maturation of muscle-like fibers. These findings reinforce the practical relevance of using reinforced, prevascularized hydrogel filaments for tissue engineering applications.

Conclusions

This study demonstrates the fabrication of mechanically robust and pre-vascularized hydrogel fibers tailored for extended culture *via* multimaterial chaotic bioprinting. Using a KSM printhead with eight inlets and two mixing elements, we fabricated filaments with intercalated layers of myoblast-laden GelMA-alginate bioink, a sacrificial material for void channel formation, and reinforcing alginate layers. This multimaterial approach enabled the rational design of constructs that balance mechanical stability, cellular functionality, and efficient mass transport.

In acellular experiments, we optimized fiber composition for mechanical robustness under agitated culture. Optimized fibers composed of 3/8 Alg_H (4%), 3/8 GelMA/Alg_L, and 2/8 HEC exhibited an elastic modulus of 12.8 kPa, retained more than 65% of their mass after 72 hours of continuous agitation, and supported long-term culture.

To illustrate the usefulness and effectiveness of this fabrication strategy to bioprint muscle-like fibers, we chaotically bioprinted C2C12 cell-laden prevascularized hydrogel filaments mechanically reinforced by only 3/8 4% Alg_H content.

The compartmentalized architecture provided by chaotic bioprinting played a pivotal role in sustaining cell viability above 90% at day 14 and facilitating cell proliferation and alignment throughout the fiber volume. Void channels enhanced mass and gas transport, alleviating nutrient and oxygen diffusion limitations within the construct and promoting cell viability and differentiation to muscle-like fibers after a culture period of 21 days.

Reinforced and prevascularized hydrogel filaments demonstrated superior cellular outcomes compared to solid filaments, which exhibited limited mass transport and concentrated cell proliferation within 200 μm near the surface.

The mechanical stability and functionality of the fabricated fibers were heavily influenced by their rationally designed compartmentalized architecture. Sacrificial layers enabled efficient mass transport, while reinforcing layers ensured the structural integrity required for extended culture periods. These features, prevascularization and mechanical reinforcement, collectively supported the alignment and multinucleation of myoblasts, crucial for muscle tissue maturation.

Remarkably, cell elongation, spreading, and a high degree of cell alignment were observed not only at the surface but also within the inner layers of prevascularized and reinforced fibers. In comparison, solid reinforced fibers lacked the mass transport capabilities provided by void channels, resulting in less uniform cell proliferation and alignment. However, the ability to tune the proportions and arrangements of inks in the chaotic bioprinting setup enabled the fabrication of hydrogel fibers with optimized mechanical and functional properties, meeting the requirements for tissue engineering applications.

These findings highlight the versatility of multimaterial chaotic bioprinting for creating complex and functional hydrogel constructs. The technique opens avenues for fabricating thick (>1 mm) tissues with robust mechanical properties, extended culture times, and high cell viability. Beyond skeletal muscle, the potential applications span various tissue engineering and regenerative medicine domains, including organ models and other thick, vascularized tissues.

In summary, chaotic bioprinting allows for the rational design and fabrication of robust, prevascularized hydrogel filaments with tunable compositions and architectures. This versatile biofabrication technique provides an effective platform for developing mature, functional constructs, paving the way for innovations in tissue engineering and regenerative medicine.

Materials and methods

Materials

Alg_H, Alg_L, HEC, calcium chloride, and DAPI were purchased from Sigma-Aldrich. Lithium phenyl-2,4,6-trimethylbenzoylphosphinate (LAP) was acquired from CELLINK. Trypsin, PBS, and antibiotic/antimycotic were obtained from Gibco, phalloidin reagent was sourced from Abcam, and Live/Dead Cell imaging kits were purchased from Invitrogen.

Preparation of hydrogels

Hydrogels for acellular experiments were prepared as follows. Alg_H was dissolved at concentrations of 2% (w/v), 4% (w/v), and 6% (w/v) in deionized water at 40 °C under continuous

stirring for 45 minutes. HEC was prepared as a 0.6% (w/v) solution in distilled water, stirred at 70 °C for 1 hour. Alg_L was dissolved at a concentration of 7% (w/v) in deionized water while stirring at 40 °C for 45 minutes.

GelMA was synthesized according to established protocols.[54] A solution containing 6% (w/v) GelMA and 0.2% (w/v) Lithium phenyl-2,4,6-trimethylbenzoylphosphinate (LAP; Allevi) was prepared in DPBS and heated at 70 °C for 15 minutes. This GelMA solution was subsequently mixed in a 1 : 1 ratio with the 7% (w/v) Alg_L solution, yielding a hybrid GelMA-based ink with a final composition of 3% (w/v) GelMA and 3.5% (w/v) Alg_L (GelMA/Alg_L). All hydrogel solutions were stored at 4 °C until further use.

Chaotic printhead fabrication

Kenics static mixer (KSM)-based printheads with varying numbers of inlets and mixing elements were designed using SolidWorks software and fabricated using a stereolithographic 3D printer (Form 3; FormLabs, Somerville, MA, USA), using Clear Resin V5 (FormLabs), as previously described by Ceballos-González et al.[31]

Printing system setup

For the fabrication of solid hydrogel filaments (i.e., filaments without channels), two inks were utilized. The first ink consisted of 4% (w/v) Alg_H, designed to provide mechanical support. The second ink comprised 3% (w/v) GelMA and 3.5% (w/v) Alg_L, intended as a cell-hosting medium. These inks were extruded independently through a KSM printhead, with each ink fed through separate ports, at flow rates ranging from 0.75 to 1 mL min^{-1}, depending on the ink composition.

For the fabrication of hydrogel filaments with channels, a sacrificial ink composed of 0.6% (w/v) HEC was always used. This sacrificial ink coextruded alongside the support ink (4% (w/v) Alg_H) and the cell-hosting ink (3% (w/v) GelMA/3.5% (w/v) Alg_L), with each ink introduced through separate feeding ports. The coextrusion process was conducted using the KSM printhead at flow rates of 0.15–0.6 mL min^{-1}, adjusted according to the specific material composition.

After printing, hydrogel filaments were crosslinked in a 2% (w/v) calcium chloride bath. For filaments containing 3% (w/v) GelMA/3.5% (w/v) Alg_L, an additional photocrosslinking step was performed under UV light (365 nm) for 45 seconds. A detailed summary of the printing conditions for hydrogel filaments with varying material compositions is provided in Table 1.

Computational simulations

Computational fluid dynamics (CFD) simulations were performed to determine flow trajectories and flow microarchitecture within multi-port printheads equipped with Kenics Static Mixer (KSM) elements. The simulations were conducted using ANSYS Fluent 2020. A fine tetrahedral mesh was employed to discretize the geometry of the system, with mesh refinement iteratively performed to ensure result convergence.

The Navier–Stokes equations were solved at each node within the 3D mesh under laminar flow conditions, assuming a transient state and no-slip boundary conditions. These simulations yielded detailed velocity field solutions for various feeding strategies, encompassing different flow rates and inlet configurations.

We took these velocity field results to conduct particle tracking to analyze individual and collective particle trajectories. A total of 100 000 massless particles were introduced per inlet, with distinct color coding applied to particles originating from different inlets. The trajectories of these particles were tracked, and their crossing patterns at the printhead outlet were recorded to determine the degree of compartmentalization and the resulting microstructure at the printhead outlet.

Analysis of fiber microstructure

Cross-sectional images of the hydrogel filaments were obtained through computational simulations and experimental imaging. For the experimental images, hydrogel filaments were fabricated using 4% (w/v) alginate solutions in three distinct colors to represent the following inks: alginate (light blue), sacrificial ink (black), and GelMA/alginate (orange). To enable detection under fluorescence microscopy, the hydrogel solutions were stained with fluorescent dyes.

Cross-section images were captured by cutting a small section of the printed filaments with a blade, wetting the sample with deionized water, and visualizing the cross-sections under an Axio Observer.Z1 microscope (Zeiss, Germany) equipped with Colibri.2 LED illumination, Apotome, and a 10× objective lens.

The proportion of each ink in the cross-section was quantified using ImageJ software. The light blue, black, and orange areas were measured, and the area fraction for each ink was calculated using eqn (1):

$$\text{Area fraction } i = (A_i/A_{\text{total}}) \tag{1}$$

where A_i is the area occupied by ink i (in pixels), and A_{total} is the total cross-sectional area of the filament (in pixels).

Tensile tests

Tensile tests were performed using a custom-built universal tensile machine equipped with a 1 kg load cell. The testing system was controlled via an Arduino-based setup, with a displacement rate set to 0.6 mm min^{-1}. Hydrogel filaments printed using a KSM printhead featuring 8 inlets and 2 mixing elements, with varying ink proportions (Fig. 2Ai and Table 3), were subjected to these tests.

For each experiment, hydrogel filaments with a diameter of 1 mm and an initial length of 30 mm were used. The Arduino system recorded displacement (mm) and force (N) data, which were subsequently processed to generate stress–strain curves using eqn (2) and (3):

$$\varepsilon = \frac{D}{L_0} \tag{2}$$

Table 3 Hydrogel fibers printed for experiments without cells

Type of KSM	Type of fiber	Nomenclature	Proportion of Alg_H	Proportion of $GelMA/Alg_L$	Proportion of HEC
Analysis of microstructure & tensile tests					
8 inlets, 2 elements	Solid fiber	Alg_H	8/8 inlets	—	—
	Hollow fiber	$GelMA/Alg_L$-HEC-Alg_H(2)	2/8 inlets	4/8 inlets	2/8 inlets
	Hollow fiber	$GelMA/Alg_L$-HEC-Alg_H(3)	3/8 inlets	3/8 inlets	2/8 inlets
	Hollow fiber	$GelMA/Alg_L$-HEC-Alg_H(4)	4/8 inlets	2/8 inlets	2/8 inlets
	Hollow fiber	$GelMA/Alg_L$-HEC-Alg_H(5)	5/8 inlets	1/8 inlets	2/8 inlets
Degradation analysis					
8 inlets, 2 elements	Hollow fiber	$GelMA/Alg_L$-HEC-Alg_H(3)	3/8 inlets	3/8 inlets	2/8 inlets
2 inlets, 4 elements	Hollow fiber	$GelMA/Alg_L$-HEC		1/2 inlets	1/2 inlets
	Solid fiber	$GelMA/Alg_L$-Alg_H	1/2 inlets	1/2 inlets	—
	Solid fiber	$GelMA/Alg_L$	—	2/2 inlets	—

where ε = strain, D = displacement (mm), L_0 = initial length (mm)

$$\sigma(kPa) = \frac{F}{A_0 \times 1000} \qquad (3)$$

where σ is the stress (kPa), F is the force (N), and A_0 is the cross-sectional area (m^2)

The elastic modulus (kPa) was determined by calculating the slope of the linear region of the stress–strain curve. Curve fitting was performed using Microsoft Excel's curve fitting function for precise determination of the modulus.

Dynamic incubation system for fiber degradation testing

A custom agitation system was developed using an Arduino UNO microcontroller to power a stepper motor. The motor was connected to a T25 culture flask *via* a 3D-printed mechanical support, facilitating continuous oscillatory motion along the horizontal axis. Each cycle consisted of 30 seconds of movement to the left followed by 30 seconds to the right, completing one minute per cycle. The entire setup was housed inside a standard incubator maintained at 37 °C with 5% CO$_2$ to ensure a controlled environment for testing.

Fiber degradation analysis

The degradation of multichannel reinforced $GelMA/Alg_L$-HEC-Alg_H fibers was evaluated and compared with control samples, as outlined in Fig. 2Bii and Table 3. The initial mass of printed fibers (devoid of cells) was measured using a high-sensitivity balance with milligram precision.

The fibers were submerged in PBS (pH 7.4) at a 1 : 1 weight-to-volume ratio (5 grams of fiber in 5 mL of PBS) within the dynamic incubation system described above. Wet mass measurements were taken at specified time points: 8, 12, 24, 48, and 72 hours.

The remaining weight percentage was calculated using eqn 4:

$$\text{Remaining mass} (\%) = \frac{m_0 - m_i}{m_0} \times 100\% \qquad (4)$$

where m_0 represents the initial mass (mg) and m_i the mass at time i (mg).

C2C12 mouse myoblast 2D culture

C2C12 mouse myoblasts (ATCC) were cultured in DMEM with high glucose (Sigma-Aldrich), supplemented with 10% (v/v) fetal bovine serum (FBS) (Gibco) and 1% (v/v) antibiotic–antimycotic solution (Gibco). Cells were maintained at 37 °C in a humidified atmosphere containing 5% CO$_2$. Once the cultures reached approximately 80% confluency in T75 flasks, they were detached using 0.25% trypsin, and the resulting cell suspension was prepared for downstream applications.

Preparation of inks

To prepare the bioinks, Alg_H was dissolved in DPBS at a concentration of 4% (w/v) and stirred at 40 °C for 45 minutes, while Alg_L was similarly dissolved at 7% (w/v) and stirred for the same duration. HEC was dissolved at a concentration of 0.6% (w/v) in DPBS and stirred at 70 °C for approximately 1 hour. GelMA was prepared as a 6% (w/v) solution containing 0.2% (w/v) LAP (photoinitiator) by dissolving the components in DPBS at 70 °C for 15 minutes. All solutions were filtered under sterile conditions using a 0.4 μm pore-size filter.

The GelMA solution was subsequently mixed with the 7% (w/v) Alg_L solution in a 1 : 1 ratio to produce a bioink containing 3% (w/v) GelMA and 3.5% (w/v) Alg_L. Before bioprinting, all bioinks were equilibrated to 37 °C to ensure compatibility with C2C12 cells. To incorporate cells, C2C12 myoblasts were detached from T75 flasks, pelleted *via* centrifugation, and resuspended in the $GelMA/Alg_L$ bioink at a final concentration of 3×10^6 cells per mL.

Chaotic bioprinting setup

Reinforced hollow fibers were fabricated using a KSM printhead with 8 inlets and 2 mixing elements. The sacrificial ink consisted of a 0.6% HEC solution, the bioink was composed of 3% GelMA, 3.5% Alg_L, and 0.5% LAP with 3×10^6 C2C12 cells per mL, and the support ink consisted of 4% Alg_H. The bioprinted fibers underwent two crosslinking steps: immersion in a 2% CaCl$_2$ bath for 1 minute to crosslink the alginate, followed by washing in PBS to remove excess CaCl$_2$. The GelMA component was then crosslinked using UV light at 365 nm for 45 seconds. After crosslinking, the fibers were cut into 1 cm segments and cultured in ultralow attachment 12-well plates

containing DMEM with 10% (v/v) FBS and 1% (v/v) antibiotic–antimycotic solution.

For the fabrication of reinforced solid fibers, a KSM print-head with 2 inlets and 4 mixing elements was used. The support ink consisted of 4% Alg$_H$, while the bioink consisted of 3% GelMA, 3.5% Alg$_L$, and 0.5% LAP with 3×10^6 live C2C12 cells per mL. A printing rate of 0.75 mL min^{-1} was employed. The fibers were crosslinked by immersion in a 2% CaCl$_2$ bath for 30 seconds, followed by a PBS wash to remove excess CaCl$_2$, and UV exposure at 365 nm for 30 seconds to stabilize the GelMA layer. As with hollow fibers, the solid fibers were cut into 1 cm pieces and cultured in ultralow attachment 12-well plates containing DMEM supplemented with 10% (v/v) FBS and 1% (v/v) antibiotic–antimycotic solution.

3D cell culture

Fiber segments measuring 5 cm in length were individually placed into the wells of a 12-well plate, each containing 4 mL of culture medium. The culture medium consisted of DMEM with high glucose, supplemented with 10% (v/v) fetal bovine serum (FBS) and 2% (v/v) antibiotic–antimycotic solution. The plate was incubated at 37 °C in a humidified atmosphere with 5% CO$_2$. On the fifth day of cultivation, the medium was replaced with DMEM supplemented with 2% (v/v) FBS and 1% (v/v) antibiotic–antimycotic solution. The culture medium was refreshed every three days, maintaining the same composition for the duration of the experiment.

Cell viability

Cell viability within solid and hollow fibers was evaluated using a Live/Dead assay following the manufacturer's protocol. Fiber segments of 1 cm in length were individually placed in 24-well plates, with one segment per well. To each well, 200 μL of Live/Dead reagent was added, prepared according to the protocol provided by the manufacturer. The fibers were incubated with the reagent at 37 °C for 30 minutes, followed by two washes with PBS to remove excess reagent. Imaging was performed using an Axio Observer.Z1 microscope (Zeiss, Germany) equipped with Colibri.2 LED illumination and an Apotome.2 system. Micrographs were captured using a 2.5× objective lens. Cell viability was assessed on days 1, 7, and 14 for both solid and hollow fibers. The results were quantified as the ratio of viable cells to the total number of cells, determined using ImageJ software with the Color Segmentation plugin.

Cell density

Cell-laden filaments were stained using Phalloidin-iFluor 647 (3:1000) and DAPI (1 μg mL^{-1}; 1:1000) to visualize actin filaments and cell nuclei, respectively. After incubation at 37 °C for 1 h, the samples were washed with PBS and visualized using an Axio Observer Z1 microscope (Zeiss, Germany). Cell density was quantified as the number of cells per unit volume (mm^3) based on Actin/DAPI-stained z-stack images. The hydrogel volume was calculated using the "Measure Area" functionality in ImageJ, while cell counts were obtained using the

"Analyze Particles" function. Circularity parameters were set between 0.2 and 1, with a size range specified to include all particles detected, from the smallest to the largest.

Cell alignment

The orientation (alignment) of myoblasts within the printed constructs was quantitatively assessed using the Directionality plugin in Fiji (ImageJ), applied to representative fluorescence micrographs obtained from Actin/DAPI staining at days 7 and 14.

Analysis was conducted using the Fourier component method, with orientation angles binned into 13 intervals ranging from −90° to +90°. Importantly, the longitudinal axis of the hydrogel filament was defined as the 0° reference, allowing us to measure the angular deviation of cells relative to the main fiber direction.

Quantitative reverse transcription PCR (RT-qPCR) assays

The expression levels of key myogenic markers—myogenin (*MyoG*) and alpha-actin 1 (*ACTA1*)—were quantified *via* reverse transcription quantitative polymerase chain reaction (RT-qPCR). *GAPDH* served as the endogenous control, and a non-template reaction was included as a negative control. Hydrogel filaments were first washed with phosphate-buffered saline (PBS), followed by enzymatic digestion using a collagenase type II solution (200 U mL^{-1}) for 10 minutes at 37 °C to degrade the hydrogel matrix and release embedded cells. The recovered cells were washed with PBS and centrifuged three times to remove debris. Total RNA was extracted using the RNeasy Micro Kit (QIAGEN), and RNA concentrations were quantified using a NanoDrop™ spectrophotometer (Thermo Scientific). Reverse transcription to complementary DNA (cDNA) was performed using the QuantiTect Reverse Transcription Kit (QIAGEN) according to the manufacturer's protocol. RT-qPCR reactions were carried out using 10 ng of cDNA per reaction, the SYBR Green PCR Kit (QIAGEN), and a Rotor-Gene Q thermal cycler. Gene expression levels were analyzed using the $2^{-\Delta\Delta CT}$ method. All reactions were run in triplicate to ensure reproducibility.

The primer sequences used were as follows: *GAPDH* (housekeeping gene): Forward: 5′-CATCACTGCCACCCAGAAGACTG-3′ and reverse: 5′-ATGCCAGTGAGCTTCCCGTTCAG-3′; *MyoG*: Forward: 5′-CAGCTCCCTCAACCAGGA-3′ and reverse: 5′-TGCCCCACTCTGGACTG-3′; and *ACTA1*: Forward: 5′-CGAT-CTCACCGACTACCTGA-3′ and reverse: 5′-CAGCTTCTCCT-TGATGTCGC-3′.

Statistical analysis

Statistical analyses were performed using one-way analysis of variance (ANOVA), followed by Tukey's test for multiple comparisons. All experimental conditions were replicated three times ($n = 3$). Statistical significance was defined as $p < 0.01$. Results are presented as the mean ± standard deviation.

Conflicts of interest

Data availability

The datasets generated and/or analyzed during the current study are not publicly available but can be requested from the corresponding authors. Requests will be considered on a reasonable basis.

Acknowledgements

References

1 S. Flores-Torres, T. Jiang, J. Kort-Mascort, Y. Yang, O. Peza-Chavez, S. Pal, A. Mainolfi, L. A. Pardo, L. Ferri, N. Bertos, V. Sangwan and J. M. Kinsella, *ACS Biomater. Sci. Eng.*, 2023, **9**, 542–561.

2 S. Madiedo-Podvrsan, J.-P. Belaïdi, S. Desbouis, L. Simonetti, Y. Ben-Khalifa, C. Collin-Djangone, J. Soeur and M. Rielland, *Sci. Rep.*, 2021, **11**, 6217.

3 A. Ahmad, S. J. Kim, Y. J. Jeong, M. S. Khan, J. Park, D. W. Lee, C. Lee, Y. J. Choi and H. G. Yi, *J. Mater. Chem. B*, 2024, **12**, 8633–8646.

4 A. Alave Reyes-Furrer, S. De Andrade, D. Bachmann, H. Jeker, M. Steinmann, N. Accart, A. Dunbar, M. Rausch, E. Bono, M. Rimann and H. Keller, *Commun. Biol.*, 2021, **4**, 1183.

5 D. Wu, S. Pang, J. Berg, Y. Mei, A. S. M. Ali, V. Röhrs, B. Tolksdorf, J. Hagenbuchner, M. J. Ausserlechner, H. E. Deubzer, A. Gurlo and J. Kurreck, *Adv. Funct. Mater.*, 2024, **34**, 2314171.

6 P. J. Tebon, B. Wang, A. L. Markowitz, A. Davarifar, B. L. Tsai, P. Krawczuk, A. E. Gonzalez, S. Sartini,

7 G. F. Murray, H. T. L. Nguyen, N. Tavanaie, T. L. Nguyen, P. C. Boutros, M. A. Teitell and A. Soragni, *Nat. Commun.*, 2023, **14**, 3168.

7 G. Janani, S. Priya, S. Dey and B. B. Mandal, *ACS Appl. Mater. Interfaces*, 2022, **14**, 10167–10186.

8 K. L. Miller, Y. Xiang, C. Yu, J. Pustelnik, J. Wu, X. Ma, T. Matsui, K. Imahashi and S. Chen, *Organs-on-a-Chip*, 2021, **3**, 100007.

9 S. Mao, J. He, Y. Zhao, T. Liu, F. Xie, H. Yang, Y. Mao, Y. Pang and W. Sun, *Biofabrication*, 2020, **12**, 045014.

10 A. A. Szklanny, M. Machour, I. Redenski, V. Chochola, I. Goldfracht, B. Kaplan, M. Epshtein, H. Simaan Yameen, U. Merdler, A. Feinberg, D. Seliktar, N. Korin, J. Jaroš and S. Levenberg, *Adv. Mater.*, 2021, **33**, 2102661.

11 A. Behre, J. W. Tashman, C. Dikyol, D. J. Shiwarski, R. J. Crum, S. A. Johnson, R. Kommeri, G. S. Hussey, S. F. Badylak and A. W. Feinberg, *Adv. Healthcare Mater.*, 2022, **11**, 2200866.

12 K. Guo, H. Wang, S. Li, P. Chang, C. He, Q. Sun and X. Zheng, *Biofabrication*, 2023, **15**, 035007.

13 J. Nulty, F. E. Freeman, D. C. Browe, R. Burdis, D. P. Ahern, P. Pitacco, Y. Bin Lee, E. Alsberg and D. J. Kelly, *Acta Biomater.*, 2021, **126**, 154–169.

14 G. Boix-Lemonche, R. M. Nagymihaly, E. M. Niemi, N. Josifovska, S. Johansen, M. C. Moe, H. Scholz and G. Petrovski, *Macromol. Biosci.*, 2023, **23**, 2200422.

15 D. Jeong, J. W. Seo, H. G. Lee, W. K. Jung, Y. H. Park and H. Bae, *Adv. Sci.*, 2022, **9**, 2202877.

16 Y. Li, W. Liu, S. Li, M. Zhang, F. Yang and S. Wang, *J. Future Foods*, 2021, **1**, 88–97.

17 S. D. Dutta, K. Ganguly, M. S. Jeong, D. K. Patel, T. V. Patil, S. J. Cho and K. T. Lim, *ACS Appl. Mater. Interfaces*, 2022, **14**, 34513–34526.

18 D. H. Kang, F. Louis, H. Liu, H. Shimoda, Y. Nishiyama, H. Nozawa, M. Kakitani, D. Takagi, D. Kasa, E. Nagamori, S. Irie, S. Kitano and M. Matsusaki, *Nat. Commun.*, 2021, **12**, 5059.

19 S. C. Pedroza-González, M. Rodriguez-Salvador, B. E. Pérez-Benítez, M. M. Alvarez and G. T. Santiago, *Int. J. Bioprint.*, 2021, **7**, 333.

20 Y. Li, X. Zhang, X. Zhang, Y. Zhang and D. Hou, *Polymers*, 2023, **15**, 3940.

21 R. Levato, O. Dudaryeva, C. E. Garciamendez-Mijares, B. E. Kirkpatrick, R. Rizzo, J. Schimelman, K. S. Anseth, S. Chen, M. Zenobi-Wong and Y. S. Zhang, *Nat. Rev. Methods Primers*, 2023, **3**, 47.

22 J. He, B. Zhang, Z. Li, M. Mao, J. Li, K. Han and D. Li, *Biofabrication*, 2020, **12**, 042002.

23 W. Long Ng and V. Shkolnikov, *Bio-Des. Manuf.*, 2024, **7**(75), 771–799.

24 K. Zheng, M. Chai, B. Luo, K. Cheng, Z. Wang, N. Li and X. Shi, *Smart Mater. Med.*, 2024, **5**, 183–195.

25 G. Yang, B. Mahadik, J. Y. Choi and J. P. Fisher, *Prog. Biomed. Eng.*, 2020, **2**, 012002.

26 X. Li and J. P. Gong, *Nat. Rev. Mater.*, 2024, **9**(96), 380–398.

27 G. Trujillo-de Santiago, M. M. Alvarez, M. Samandari, G. Prakash, G. Chandrabhatla, P. I. Rellstab-Sánchez, B. Byambaa, P. P. S. S. Abadi, S. Mandla, R. K. Avery, A. Vallejo-Arroyo, A. Nasajpour, N. Annabi, Y. S. Zhang and A. Khademhosseini, *Mater. Horiz.*, 2018, **5**(5), 813–822.

28 C. Chávez-Madero, M. D. De León-Derby, M. Samandari, C. F. Ceballos-González, E. J. Bolívar-Monsalve, C. Mendoza-Buenrostro, S. Holmberg, N. A. Garza-Flores, M. A. Almajhadi, I. González-Gamboa, J. F. Yee-de León, S. O. Martínez-Chapa, C. A. Rodríguez, H. K. Wickramasinghe, M. Madou, D. Dean, A. Khademhosseini, Y. S. Zhang, M. M. Alvarez and G. Trujillo-de Santiago, *Biofabrication*, 2020, **12**, 035023.

29 G. Trujillo-de Santiago and M. M. Alvarez, *Aggregate*, 2024, **5**, e548.

30 M. Samandari, F. Alipanah, K. Majidzadeh-A, M. M. Alvarez, G. Trujillo-de Santiago and A. Tamayol, *Appl. Phys. Rev.*, 2021, **8**, 021404.

31 C. F. Ceballos-González, E. J. Bolívar-Monsalve, D. A. Quevedo-Moreno, C. Chávez-Madero, S. Velásquez-Marín, L. L. Lam-Aguilar, Ó.E Solís-Pérez, A. Cantoral-Sánchez, M. Neher, E. Yzar-García, Y. S. Zhang, C. Gentile, A. R. Boccaccini, M. M. Alvarez and G. Trujillo-de Santiago, *Adv. Mater. Technol.*, 2023, **8**, 2202208.

32 E. J. Bolívar-Monsalve, C. F. Ceballos-González, C. Chávez-Madero, B. G. Cruz-Rivas, S. V. Marín, S. Mora-Godínez, L. M. Reyes-Cortés, A. Khademhosseini, P. S. Weiss, M. Samandari, A. Tamayol, M. M. Alvarez and G. Trujillo-de Santiago, *Adv. Healthcare Mater.*, 2022, **11**(24), 2200448.

33 L. E. Freed, C. Vunjak-Novakovic and R. Langer, in *Cultivation of Cell-Polymer Cartilage Implants in Bioreactors*, 1993, vol. 51.

34 A. Khodabukus, N. Prabhu, J. Wang and N. Bursac, *Adv. Healthcare Mater.*, 2018, **7**, 1701498.

35 S. Kim, B. Ayan, M. Shayan, T. A. Rando and N. F. Huang, *Stem Cell Rep.*, 2024, **19**, 1061–1073.

36 R. Mestre, N. García, T. Patiño, M. Guix, J. Fuentes, M. Valerio-Santiago, N. Almiñana and S. Sánchez, *Biofabrication*, 2021, **13**, 045011.

37 G. Agrawal, A. Aung and S. Varghese, *Lab Chip*, 2017, **17**, 3447.

38 J. M. Fernández-Costa, A. Tejedera-Vilafranca, X. Fernández-Garibay and J. Ramón-Azcón, *Dis. Models Mech.*, 2023, **16**(6), dmm050107.

39 Y. Dou, L. Zhang, J. Wang, Y. Xue, Y. Zhou, Y. Liu, L. Zhang and R. Shi, *Tissue Eng., Part C*, 2024, **30**, 130–141.

40 S. Sabetkish, P. Currie and L. Meagher, *Acta Biomater.*, 2024, **181**, 46–66.

41 F. B. Albrecht, T. Ahlfeld, A. Klatt, S. Heine, M. Gelinsky and P. J. Kluger, *Adv. Healthcare Mater.*, 2024, **13**, 2304058.

42 N. Moghimi, M. Kamaraj, F. Zehtabi, S. A. Yavari, M. Kohandel, A. Khademhosseini and J. V. John, *J. Mater. Chem. B*, 2024, **12**, 2818–2830.

43 S. Jiang, H. Jing, Y. Zhuang, J. Cui, Z. Fu, D. Li, C. Zhao, U. Liaqat and K. Lin, *Carbohydr. Polym.*, 2024, **332**, 121933.

44 M. S. Toftdal, N. P. Christensen, F. B. Kadumudi, A. Dolatshahi-Pirouz, L. G. Grunnet and M. Chen, *J. Colloid Interface Sci.*, 2024, **667**, 54–63.

45 K. Yue, G. Trujillo-de Santiago, M. M. Alvarez, A. Tamayol, N. Annabi and A. Khademhosseini, *Biomaterials*, 2015, **73**, 254–271.

46 M. M. Alvarez, A. Cantoral-Sánchez and G. Trujillo-de Santiago, *Adv. Drug Delivery Rev.*, 2025, **216**, 115475.

47 C. Ort, Y. Chen, A. Ghagre, A. Ehrlicher and C. Moraes, *ACS Biomater. Sci. Eng.*, 2021, **7**, 2814–2822.

48 A. Serafin, C. Murphy, M. C. Rubio and M. N. Collins, *Mater. Sci. Eng.*, 2021, **122**, 111927.

49 X. Zhou, Q. Gao, D. Yu, Y. Shao, Z. Wang, X. Liu, W. Wang, L. Chang, T. Ma, H. Mok, J. Cen, J. Chen, M. El Tahchi, J. Zhuang, F. Mou, J. Zhang and Y. Yin, *Smart Mater. Med.*, 2022, **3**, 199–208.

50 C. F. Ceballos-González, E. J. Bolívar-Monsalve, D. A. Quevedo-Moreno, L. L. Lam-Aguilar, K. I. Borrayo-Montaño, J. F. Yee-De León, Y. S. Zhang, M. M. Alvarez and G. Trujillo-de Santiago, *ACS Biomater. Sci. Eng.*, 2021, **7**, 2408–2419.

51 E. J. Bolívar-Monsalve, C. F. Ceballos-González, K. I. Borrayo-Montaño, D. A. Quevedo-Moreno, J. F. Yee-de León, A. Khademhosseini, P. S. Weiss, M. M. Alvarez and G. Trujillo-de Santiago, *Bioprinting*, 2021, **21**, e00125.

52 Z. Xuan, Q. Peng, T. Larsen, L. Gurevich, J. de Claville Christiansen, V. Zachar and C. P. Pennisi, *Tissue Eng. Regener. Med.*, 2023, **20**, 199–212.

53 J. Stern-Straeter, G. A. Bonaterra, S. S. Kassner, S. Zügel, K. Hörmann, R. Kinscherf and U. R. Goessler, *J. Tissue Eng. Regener. Med.*, 2011, **5**, e197–e206.

54 J. A. Tavares-Negrete, S. C. Pedroza-González, A. I. Frías-Sánchez, M. L. Salas-Ramírez, M. d. l. Á. de Santiago-Miramontes, C. M. Luna-Aguirre, M. M. Alvarez and G. Trujillo-de Santiago, *ACS Biomater. Sci. Eng.*, 2023, **9**(6), 3462–3475.